CHAPTER-5

Photoredox molecular oxygen activation with lead-free metal halide perovskite for oxidative amidation of alcohols

5.1. Introduction

Following the successful utilization of $CsPbBr_3$ for the photoredox C–N coupling and THIQ semidehydrogenation via H_2O_2 production mechanism, we focus on the development of lead-free halide perovskite for oxidative amidation of alcohols.

Amides are key functional groups in polymers, drugs, biomolecules, agrochemicals, and natural products.[1-4] Traditionally, amides were formed from amines and carboxylic acid derivatives;[5] they can also be synthesized via Schmidt, Ugi, Staudinger, and Ritter reactions.[2,5-9] Due to limitations, safer methods, such as catalytic oxidative amidation, amide transamination, and amine acylation, have emerged.[10,11] Notably, catalytic oxidative amidation of benzaldehydes or benzyl alcohols with amines offers an eco-friendly alternative.[1]

Photocatalytic amidation using Ru-, Ir-based, and organic photocatalysts (e.g., phenazine salts, rose Bengal, acridinium salt) has shown high selectivity,[12-19] but is limited by cost, metal dependency, and poor recyclability. Visible-light-driven semiconductor catalysts like Ag/g-C_3N_4, Ni/g-C_3N_4, Mn_3O_4, TiO_2, and Pd/MIL-101(Fe) offer better recyclability,[14,16,18,19] yet often suffer from low active sites, rapid charge recombination, and narrow light absorption.

Amidation of benzyl alcohols with amines is a sustainable alternative, using abundant, low-toxic, and inexpensive alcohols over aldehydes. Milstein's group first used Ru pincer complexes for this via hydrogen atom transfer (HAT).[20] Later, HAT-based methods with metal catalysts were developed,[21,22] but often need high temperatures, excess oxidants, and bases. Yin's group introduced a milder photocatalytic method using Ag_2O/P-C_3N_4.[13]

Halide perovskites are promising photocatalysts for energy conversion and organic reactions due to tunable band gaps, high charge mobility, and low exciton binding energy.[23-29] Pb-based perovskites like $CsPbBr_3$ are well-studied but limited by toxicity and water

sensitivity, driving interest in lead-free alternatives with strong photoredox activity.[30] Dong et al. showed that Cs_2CuBr_4 outperforms $CsPbBr_3$ in CO_2 photoreduction.[31] Copper's variable valence and d-band tuning, along with surface Cu^{2+}/Br^- Lewis pair sites, enhance substrate adsorption via frustrated Lewis pair interactions.[32-35]

The unique properties of Cs_2CuBr_4 have inspired us to investigate its photoredox activity in organic transformation reactions. Additionally, we have modified the band structure of Cs_2CuBr_4 by adjusting the synthesis methods. The hot injection method yields PC-1, which features smaller nanoparticles compared to the room temperature method (PC-2). The nanoparticle size significantly impacts the bandgap (PC-1: 1.89 eV vs. PC-2: 1.64 eV) and band positions (CBM_{PC-1}: -0.80 eV vs. CBM_{PC-2}: -0.72 eV, VBM_{PC-1}: 1.09 eV vs. VBM_{PC-2}: 0.92 eV). Furthermore, PC-1 demonstrates improved charge separation and transfer, with less recombination of photo-generated charge carriers than PC-2.

The conduction band minimum of Cs_2CuBr_4 (PC-1) is sufficiently negative (-0.80 V vs. NHE) to reduce O_2 to $O_2^{\bullet-}$ (-0.33 V vs. NHE), promoting superoxide radical formation via electron transfer. Prior studies on lead halide perovskites show that O_2 adsorbs via van der Waals forces, and subsequent electron transfer forms strong Pb–O bonds, causing structural degradation. However, O_2 exposure under light also enhances photoluminescence lifetime and quantum yield, indicating that O_2 can modulate perovskite optoelectronic properties by influencing charge-transfer dynamics.

The more negative conduction band of PC-1 enables efficient O_2 reduction to $O_2^{\bullet-}$ radicals, initiating benzyl alcohol dehydrogenation. Its more positive valence band also promotes amine oxidation via hole transfer. Together, these properties make PC-1 highly effective for oxidative amidation of alcohols with amines, achieving amide product yields of up to 98%. Additionally,

PC-1 retains activity over five reuse cycles with minimal loss.

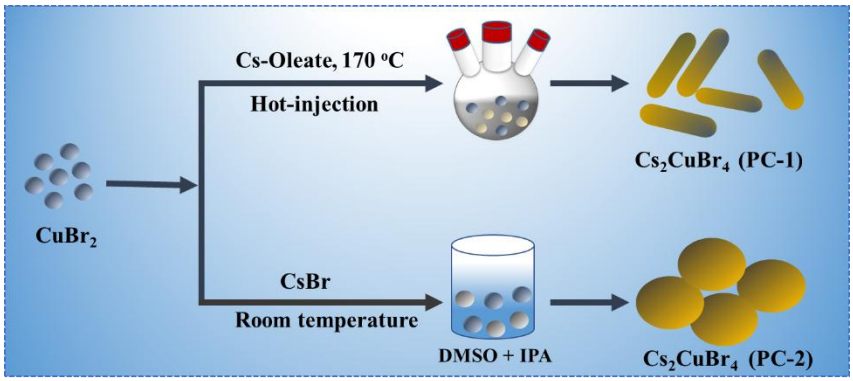

Scheme 5.1. Schematic representation showing the structural modulation of Cs_2CuBr_4 by two different synthesis methods: (i) Hot-injection (PC-1) and (ii) Room temperature (PC-2).

5.2. Chemicals

All the chemical details were mentioned in Chapter 2, Section 2.2.

5.3. Instrumentation

The same instruments were used for the spectroscopic, microscopic, and NMR characterization of the catalysts and products as mentioned in Chapter 2, Section 2.3.

5.4. Experimental

5.4.1. Synthesis of Cs_2CuBr_4 by hot injection method (PC-1)

Initially, a Cs-OA precursor stock solution was prepared by adding Cs_2CO_3 (203 mg), ODE (10 mL), and OA (0.5 mL) in a 50 mL three-neck flask, heated at 120 °C for 1 hour under an N_2 atmosphere. Subsequently, $CuBr_2$ (1 mmol), ODE (10.0 mL), OAm (1.0 mL), and OA (1.0 mL) were introduced into a 25 mL three-neck flask and dried at 120 °C for 1 hour under an N_2 atmosphere. The temperature was then raised to 170 °C, and the Cs-OA stock solution (0.5 mL) was rapidly injected and stirred for 1 minute to attain complete solubility. The resulting reaction mixture was promptly cooled down by placing the flask in an ice-water bath. The precipitate was isolated via centrifugation, washed with acetone, and dispersed in toluene for

subsequent utilization, which was named PC-1(**Scheme 5.1**).

5.4.2. Synthesis of Cs_2CuBr_4 at room temperature (PC-2)

Cs_2CuBr_4 was prepared by dissolving 212 mg of CsBr (1.0 mmol) and 111.67 mg of $CuBr_2$ (0.5 mmol) in 20 mL of DMSO to create a homogeneous precursor solution. This solution was introduced into 50 mL of isopropanol under vigorous stirring, leading to the completion of the reaction within 1 minute. Further centrifugation at 10000 rpm for 5 minutes to obtain the final product named PC-2.[2] The PC-2 particle size varies with the amount of isopropanol, which is crucial because it initiates both nucleation and particle growth. However, increasing the amount of isopropanol leads to smaller particle sizes due to slower nucleation, with the synthesis temperature maintained at 35±2 °C.

Table 5.1. Description of the photocatalysts

S.N.	Photocatalyst	Synthesis methods	Catalyst named
1	Cs_2CuBr_4	Hot-injection	PC-1
2	Cs_2CuBr_4	Room temperature	PC-2

5.5. Results and discussion

5.5.1. Syntheses and characterizations of the catalysts

Previously, Cs_2CuBr_4 was synthesized using a room temperature method.[40,41] In this study, we developed a hot injection method to obtain smaller Cs_2CuBr_4 nanoparticles (PC-1) compared to the room temperature variant (PC-2) (**Scheme 5.1**).[26,27] PXRD analysis confirmed the orthorhombic structure (JCPDS: 71-1462, space group Pnma; **Figure 5.1a**).[31] Notably, PXRD peaks of PC-1 showed a positive shift relative to PC-2. During hot injection, oleylamine acts as an anti-aggregation agent by coordinating to the surface of the growing nanocrystals, providing steric stabilization and preventing particle agglomeration. IR spectra of PC-1

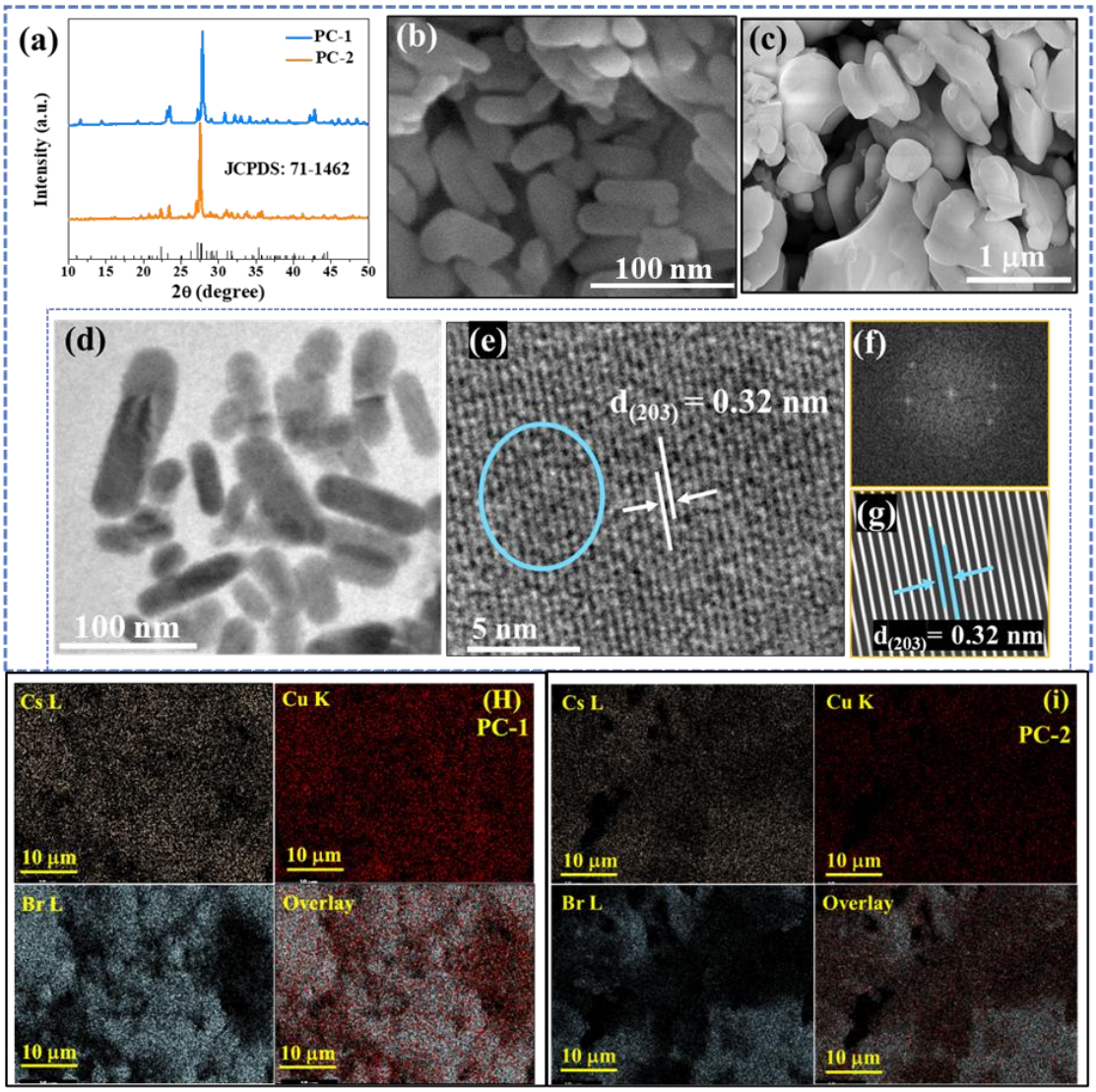

Figure 5.1. (a) PXRD patterns of PC-1 and PC-2 matched with JCPDS no. 71-1462. (b and c) SEM image showing the rod shape morphology of PC-1 and PC-2; (d) TEM image of PC-1, showing nanorod morphology. (e) High-resolution TEM image showing the lattice spacing corresponding to the (203) plane of Cs_2CuBr_4. (f) Fast Fourier transform (FFT) and (g) inverse FFT corresponding to the selected circle area of (e). (H and i) Elemental mapping of PC-1 and PC-2 showing the uniform distribution of Cs, Cu, and Br.

revealed N–H stretching bands from oleylamine.[41] While oleylamine reduces non-radiative recombination and enhances photoluminescence and stability, it can also passivate the surface, limiting substrate interaction.[42,43]

Scanning electron microscopy (SEM) revealed large, irregular particles (>500 nm) for PC-

2, while PC-1 showed rod-shaped particles (**Figure 5.1b-c**). Transmission electron microscopy (TEM) confirmed the rod-like morphology of PC-1 with sizes ranging from 100–200 nm (**Figure 5.1d**).[31,39,40] High-resolution TEM (HRTEM) showed a lattice spacing of 0.32 nm, corresponding to the (203) plane of Cs_2CuBr_4 (**Figure 5.1e**). Fast Fourier transform (FFT) and inverse FFT further validated this crystallographic plane (**Figure 5.1f-g**). Energy-dispersive X-ray (EDX) spectra of both PC-1 and PC-2 confirmed the presence of Cs, Cu, and Br, with elemental mapping indicating uniform distribution of all elements (**Figure 5.1h-i**).

The change in the Cs_2CuBr_4 synthesis process not only shifts PXRD peaks but also alters the electronic structure, as shown by X-ray photoelectron spectroscopy (XPS). The Cs 3d spectrum was deconvoluted into Cs $3d_{5/2}$ and Cs $3d_{3/2}$ peaks (**Figure 5.2a**), with a 0.49 eV positive shift in Cs $3d_{5/2}$ for PC-1, indicating reduced electron density around Cs. Similarly, the Cu 2p spectrum (**Figure 5.2b**) showed a 0.62 eV shift in the Cu $2p_{3/2}$ peak for PC-1. The Cu^{2+}/Cu^{+} ratio was higher in PC-1 (2.65) than in PC-2 (1.31), supported by a lower spin-orbit coupling value (21.69 eV vs. 22.24 eV). This higher Cu^{2+} content enhances the Lewis acidity, promoting substrate adsorption. Additionally, the Br 3d peak in PC-1 shifted by 0.53 eV to higher binding energy (**Figure 5.2c**). These electronic structure changes contribute to improved photocatalytic performance in the oxidative amidation of alcohols and amines.

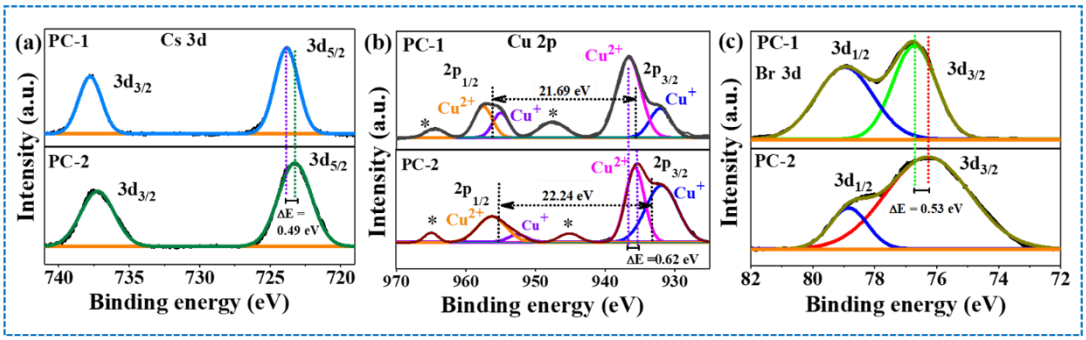

Figure 5.2. Comparison of XPS of PC-1 and PC-2, showing in figure (a) Cs 3d, (b) Cu 2p, (c) Br 3d. XPS of Cs, Cu, and Br showed a positive shift of the peaks in PC-1 compared to PC-2 because of the structural modulation.

5.6. Optoelectronic properties of the photocatalysts

UV-visible diffuse reflectance spectroscopy (DRS) revealed the light absorption and bandgap properties of Cs_2CuBr_4 samples (**Figure 5.3a**).[31,44] Tauc plots showed band gaps of 1.81 eV for PC-1 and 1.64 eV for PC-2 (inset, **Figure 5.3a**). PC-1 exhibited a blue-shifted absorption edge, indicating absorption of higher-energy light.[31,44,45]

Mott-Schottky analysis showed positive slopes in the 0.5–1.5 kHz range, confirming both samples as n-type semiconductors (**Figure 5.3b-c**).[31,44,45] The Fermi levels (E_f) were -0.70 eV for PC-1 and -0.62 eV for PC-2. Correspondingly, the valence band maxima (VBM) were calculated as 1.09 V and 0.92 V vs. NHE for PC-1 and PC-2, respectively (**Figure 5.3d**). The

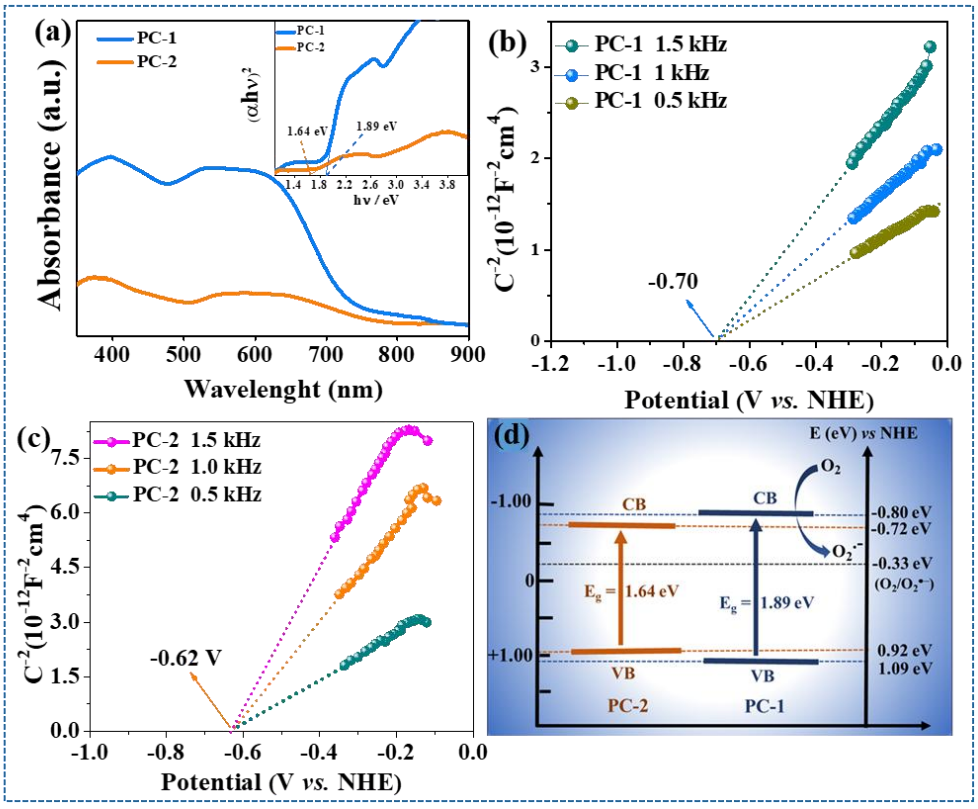

Figure 5.3. (a) The UV-vis. diffuse reflectance spectra of PC-1 and PC-2, inset showing the corresponding Tauc plot, demonstrating a significant change in the band gap for PC-1 and PC-2. (b and c) Mott-Schottky plot of PC-1 and PC-2. (d) The conduction band minima and valence band maxima for PC-1 and PC-2, derived from Tauc plot and Mott–Schottky studies.

electronic band structure critically influences photocatalytic activity. PC-1, with a wider bandgap (1.89 eV) than PC-2 (1.64 eV), demonstrates more efficient photon energy utilization. The more negative CBM further aids in activating molecular oxygen to generate superoxide radicals, initiating C–N coupling for amide formation.

To probe the electronic structure, cyclic voltammetry (CV) and differential pulse voltammetry (DPV) were conducted under dark and light conditions (**Figure 5.4a**). While light had minimal effect on peak positions (**Figure 5.4a**), PC-1 displayed more negative reduction peaks than PC-2, indicating enhanced oxygen activation capability during photocatalysis.

The photoluminescence (PL) spectrum of Cs_2CuBr_4 showed an emission peak around 460

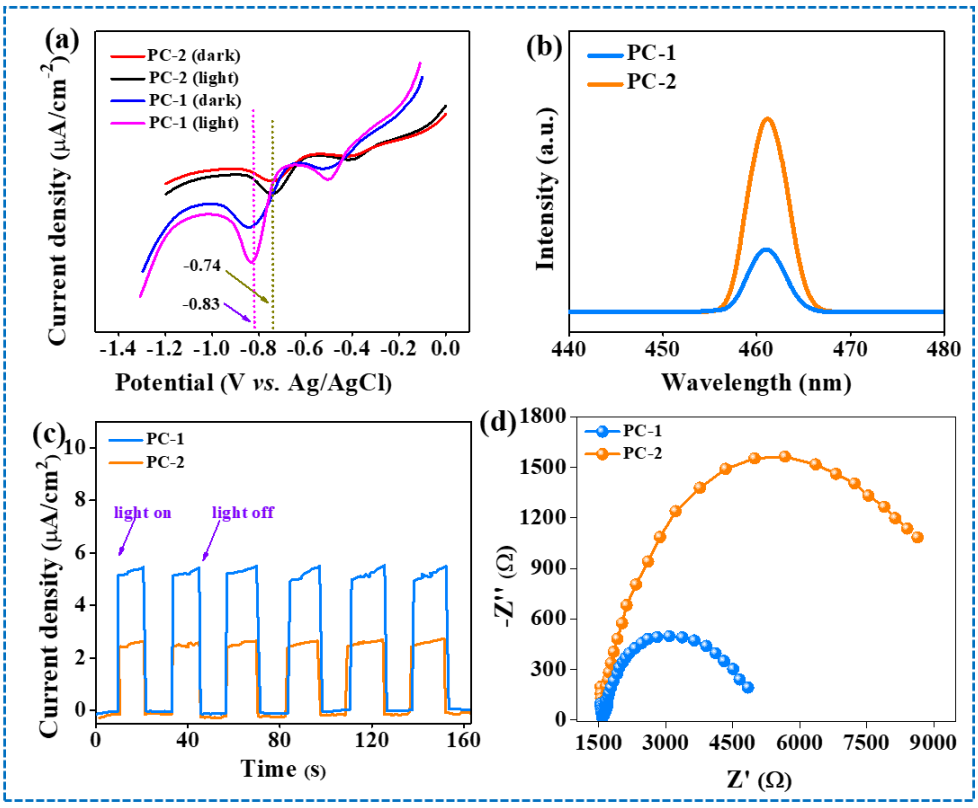

Figure 5.4. (a) Differential pulse voltammograms (DPV) of PC-1 and PC-2 were recorded under dark and illuminated conditions. (b) Photoluminescence spectra indicating reduced charge carrier recombination in PC-1 compared to PC-2. (c) Transient photocurrent responses under light/dark cycles, demonstrating enhanced charge separation efficiency in PC-1. (d) Electrochemical impedance spectra under illumination, showing lower charge transfer resistance for PC-1 relative to PC-2.

nm for both catalysts (**Figure 5.4b**), but with significantly lower intensity for PC-1, suggesting faster charge carrier dynamics.[48-50,51] Photocurrent measurements confirmed superior charge separation and transport in PC-1 compared to PC-2 (**Figure 5.4c**).[52-55] Electrochemical impedance spectroscopy (EIS) under light further revealed lower charge transfer resistance for PC-1 (**Figure 5.4d**).[31,39,40,44-46] These findings suggest that the smaller particle size of PC-1 shortens the migration path of photogenerated carriers, enhancing carrier density and improving generation and separation efficiency.

5.7. Optimization of reaction conditions for the amidation of alcohols

Photocatalytic amidation of alcohols with various amines under visible light using PC-1 and PC-2 yielded amides (**Table 5.2**). Optimization was carried out using 4-nitrobenzyl alcohol and pyrrolidine. PC-1 showed superior activity, producing 4-nitrophenyl(pyrrolidine-1-yl)methanone with a 97% yield (**Entry 1, Table 5.2**), while PC-2 gave only 74% under identical conditions and reached 94% even after 15 hours. To further validate PC-1's enhanced performance, reactions involving 4-nitrobenzyl alcohol with piperidine and 2-pyridine methanol with pyrrolidine were performed. In all cases, PC-1 consistently delivered higher amide yields than PC-2 (**Entry 1, Table 5.2**).

Molecular oxygen plays a critical role in the amidation reaction, as no amide formation occurs under N_2. In air, O_2 is reduced to superoxide radicals via photogenerated electrons from the CB of Cs_2CuBr_4 (**Figure 5.3d**), which then initiate benzyl alcohol dehydrogenation. Without O_2, the reaction does not proceed. The reaction is faster under pure O_2 than in air (**Table 5.3**). In the dark, the yield drops to just 4%, and no product forms without the catalyst. Among the tested solvents, tetrahydrofuran (THF) gave the best results (**Table 5.3**).

Table 5.2. Comparison of the photocatalytic activities of PC-1 and PC-2 for the amidation of alcohols in the presence of light.

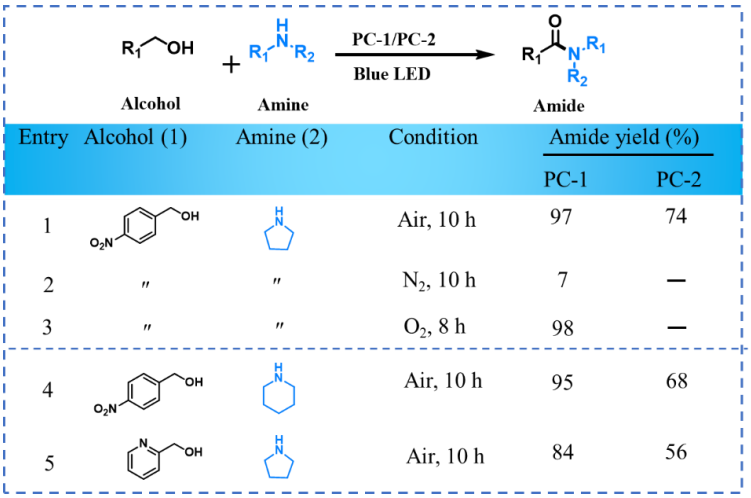

Entry	Alcohol (1)	Amine (2)	Condition	Amide yield (%)	
				PC-1	PC-2
1			Air, 10 h	97	74
2	〃	〃	N_2, 10 h	7	—
3	〃	〃	O_2, 8 h	98	—
4			Air, 10 h	95	68
5			Air, 10 h	84	56

Reaction conditions: alcohol (0.5 mmol), amine (1.0 mmol), photocatalyst (10 mg) in THF (3 mL), irradiated with a 15 W blue LED at 35 ± 2 °C for 10 hours. Products were isolated and purified, with yields reported. Structural confirmation and purity were assessed by ^{1}H and ^{13}C NMR spectroscopy.

5.8. Substrate scope for the amide synthesis

The amide bond formation using alcohol derivatives and secondary amines showed broad substrate scope and high functional group tolerance, delivering excellent yields. Various benzyl alcohols were reacted with pyrrolidine under optimized conditions to produce a series of amides (**Table 5.4, 5a-5k**). Substituents on the aromatic ring significantly affected the yields, electron-donating groups such as 4-methyl and 4-methoxy led to lower amide yields (**Table 5.4, 5b–5c**).

The electron-donating 3,4,5-trimethoxy groups on the phenyl ring of benzyl alcohol reduced amide yield (**Table 5. 4, 5d**). In contrast, electron-withdrawing groups at the para-position, such as $–NO_2$, –Cl, and $–CF_3$, significantly enhanced amide yields (**Table 5.4**, **5e, 5g, 5h**), with 4-chlorobenzyl alcohol yielding 95% (**Table 5.4**, **5g**). However, when these groups were at the ortho-position, yields decreased (**Table 5.4, 5f, 5i**). The method also proved

Table 5.3. Optimization of the reaction conditions for photocatalytic amination of alcohols.

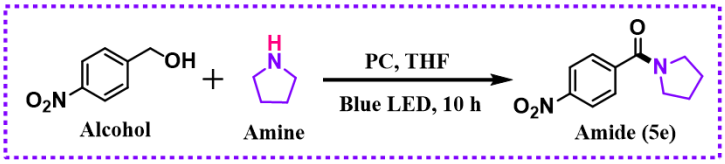

S.N.	Photocatalyst	Solvent	Conditions	Light	Time (h)	Yield (%)
Variation of catalysts						
1	PC-1	THF	air	Blue LED	10	97
2	PC-2	THF	air	Blue LED	10	74
Variation of solvents						
3	PC-1	Acetonitrile	air	Blue LED	10	67
4	**PC-1**	**THF**	**air**	**Blue LED**	**10**	**97**
5	PC-1	1,4-Dioxane	air	Blue LED	10	84
6	PC-1	Toluene	air	Blue LED	10	63
7	PC-1	Methanol	air	Blue LED	10	27
8	PC-1	Ethanol	air	Blue LED	10	22
9	PC-1	DMSO	air	Blue LED	10	58
Other variations in the reaction conditions						
10	-	THF	air	Blue LED	10	No Reaction
11	PC-1	THF	air	Dark	10	~ 4
12	PC-1	THF	N_2	Blue LED	10	No Reaction
13	PC-1	THF	Pure O_2	Blue LED	8	98

Reaction conditions: 4-nitrobenzyl alcohol (0.5 mmol), pyrrolidine (1.0 mmol), photocatalyst (PC-1 or PC-2, 10 mg), solvent (3 mL), under air, irradiated with a 15 W blue LED at 35 ± 2 °C for 10 hours. The photocatalyst was recovered by centrifugation at 13,000 rpm for 15 minutes. Products were purified using silica gel column chromatography with varying ratios of ethyl acetate and hexane. Product identity and purity were confirmed by ^{1}H and ^{13}C NMR spectroscopy, and isolated yields are reported.

effective for heterocyclic alcohols, giving amide yields above 82%, though still lower than those from benzyl alcohols (**Table 5.4, 5j 5k**).

The variation of the amine also affected the amide yields. When 2-oxazolidine or morpholine reacted with 4-nitrobenzyl alcohol, amide yields were significantly lower than with pyrrolidine (**Table 5.4, 5e vs 5l and 5m**), while piperidine gave similar yields (**Table 5.4, 5k**).

Interestingly, 2-aminopyridine, a heteroaromatic amine, yielded 76% amide with 4-nitrobenzyl alcohol (**Table 5.4, 5o**). In contrast, aniline resulted in a reduced yield (**Table 5.4, 5p**), and benzylamine produced 71% amide when reacted with benzyl alcohol (**Table 5.4, 5q**). However, when 4-nitrobenzyl alcohol reacted with the open-chain aliphatic amine diethylamine, the yield decreased (**Table 5.4, 5r**). The NMR data are mentioned in **Table 5.5**.

Table 5.4. Substrate scope evaluation using various alcohols and amines for amide bond synthesis.

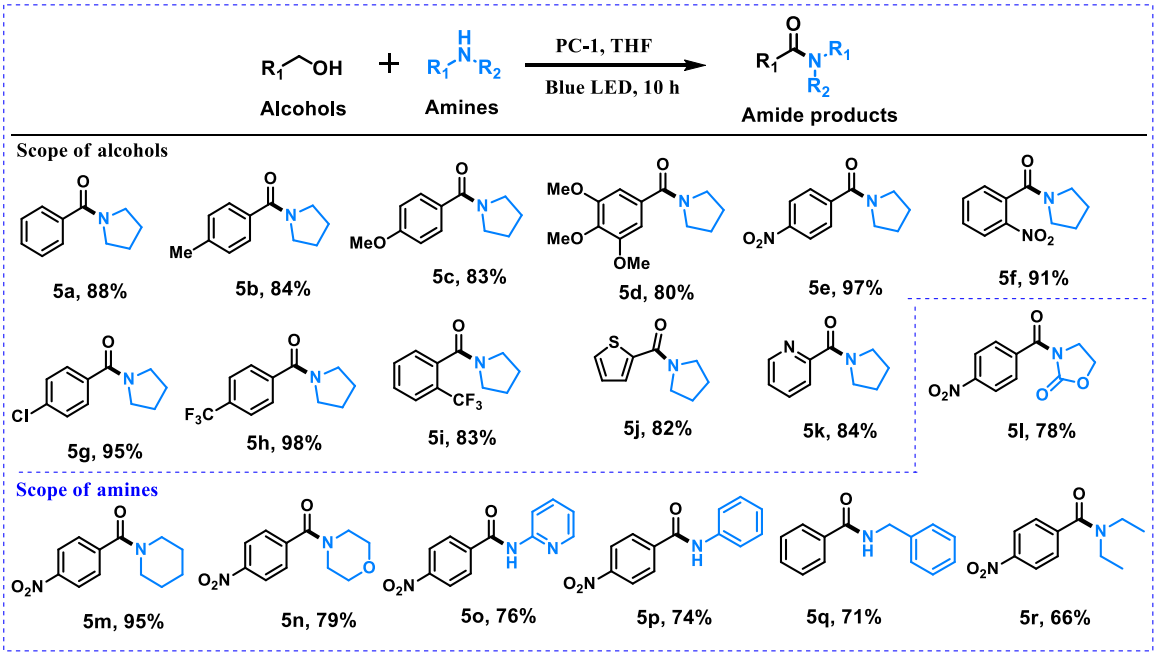

Reaction conditions: alcohol (0.5 mmol), amine (1.0 mmol), PC-1 (10 mg) in THF (3 mL), under air, irradiated with a 15 W blue LED at 35 ± 2 °C for 10 hours. In all cases, isolated product yields were reported, and product structures were confirmed by ^{1}H and ^{13}C NMR spectroscopy.

5.9. Reaction mechanism

Based on control experiments and the identification of reaction intermediates, a mechanism for the photocatalytic amidation of alcohols is proposed **(Figure 5.5a)**. Upon visible light irradiation, excitons are generated, followed by their separation and migration. The photogenerated electrons from the CB of Cs_2CuBr_4 are transferred to molecular oxygen and produce $O_2^{\bullet-}$. The formation of the C–N bond proceeds through two main steps: (i) single-

electron reduction of O_2 to form $O_2^{\bullet-}$ and (ii) oxidation of the amine to a cationic radical (**2e***) via valence band holes (h^+). PC-1, with a more negative CBM (E_{CB} = −0.80 V vs NHE at pH 7) than PC-2, favors the reduction of O_2 to $O_2^{\bullet-}$ ($O_2 + e^- \rightarrow O_2^{\bullet-}$, E° = −0.33 V vs NHE, pH 7) **(see Figure 5.3d)**. The resulting $O_2^{\bullet-}$ radicals promote the dehydrogenation of 4-nitrobenzyl alcohol, generating a 4-nitrobenzyl radical (**1e***) and hydroperoxyl radical ($^{\bullet}OOH$). Due to the lower bond dissociation energy of the Cα−H bond (79.3 kcal/mol) compared to the O−H bond (99.0 kcal/mol), $O_2^{\bullet-}$ preferentially abstracts hydrogen from the Cα−H position.[56] Next, radical coupling between **1e*** and **2e*** yields an intermediate species (**I**$^{\#}$), which undergoes deprotonation by $^{\bullet}OOH$ to form A* and H_2O_2. Finally, the reaction of $O_2^{\bullet-}$ with A* leads to the formation of the final product (**5e**) along with another equivalent of H_2O_2 **(Figure 5.5a)**.

As reported in previous studies, Copper(I)/(II) redox pairs synergistically enhance C–N coupling efficiency and selectivity: Cu(I) initiates oxidative addition and nucleophilic attack, while Cu(II) enables redox transformations, regenerates Cu(I), and stabilizes reactive intermediates.[57-59]

In contrast, oxidation of 4-nitrobenzyl alcohol to 4-nitrobenzaldehyde was not observed in the presence of pyrrolidine, but occurred slowly without amine (**Figure 5.5b**), ruling out the aldehyde–amine route to amide. Supporting this, the reaction of 4-nitrobenzaldehyde with pyrrolidine was slower than that of 4-nitrobenzyl alcohol with pyrrolidine. While oxidation of 4-nitrobenzyl alcohol alone was also slow, it was still faster than the aldehyde–amine reaction. These findings confirm that amide formation proceeds via radical coupling of intermediates **1e*** and **2e***, not through aldehyde intermediacy (**Figure 5.5b**).

5.10. Quenching experiments

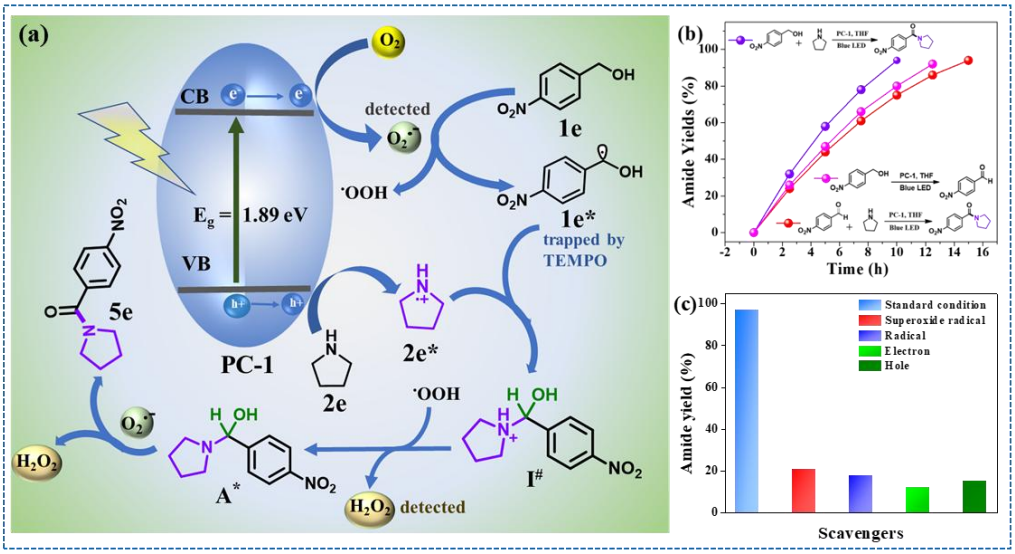

Figure 5.5. (a) The proposed mechanism for photocatalytic oxidative amidation of alcohol is based on the detected intermediates. (b) Difference in the rate of the reactions for C–N bond formation. (c) Quenching experiments confirmed the radical process involved in the amide bond formation reaction.

Further, a series of quenching experiments were carried out to understand the involvement of the electrons from the CB, holes from the VB, and $O_2^{\bullet-}$ radicals (**Figure 5.5c**). The addition of $AgNO_3$ and triethylamine as the electron and hole scavengers resulted in a significant drop in the yield of 3e to 12% and 15 %, respectively.[60] when 4-benzoquinone (BQ) was used as an $O_2^{\bullet-}$ scavenger, the yield of amide decreased to 21% (**Figure 5.5c**).[61–63]

In addition, the involvement of the radical mechanism was proved by the radical trapping reaction. In the presence of TEMPO, the yield of 5e was reduced to 18% (**Figure 5.5c**). Further, we are able to detect TEMPO-1e* and TEMPO-2e* adducts by mass spectrometry. The production of $O_2^{\bullet-}$ was detected by the *p-Nitro*-Blue tetrazolium chloride (NBT) test (**Figure 5.6a**).[64] The UV-visible spectroscopy confirmed (NBT test) that PC-1 produces more $O_2^{\bullet-}$ compared to PC-2.[65] The formation of H_2O_2 was also detected by using *o*-tolidine as an indicator (**Figure 5.6b**).[66–68] Therefore, it is clear that PC-1 is more effective in the activation of molecular oxygen compared to PC-2 (**Figure 5.6a-b**). The photocurrent and PL study

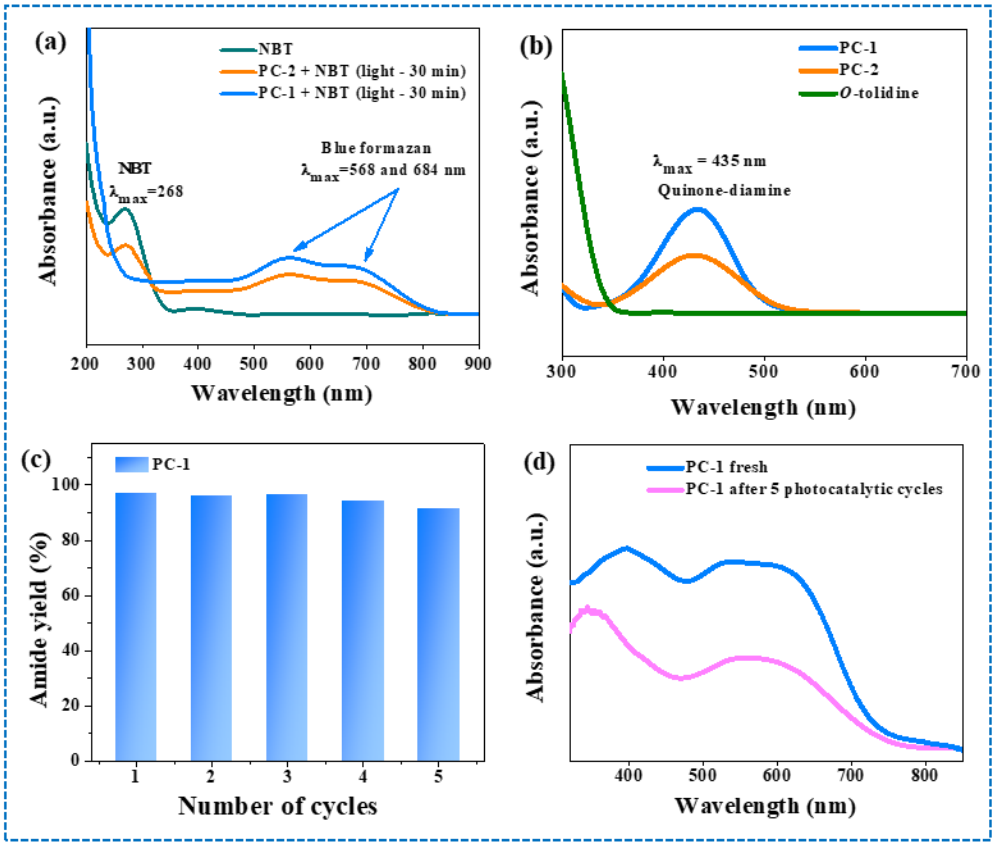

Figure 5.6. (a) Detection of photogenerated superoxide radicals. (b) UV-visible spectroscopic detection of photogenerated H_2O_2 in the reaction mixture. (c) Recyclability of PC-1 photocatalyst for amide bond formation reaction. (d) UV-vis-DRS of PC-1 after five cycles and before catalysis

revealed that PC-1 nanoparticles showed improved photocatalytic activity compared to that of PC-2.

The stability of the catalyst was assessed over five recycling cycles, showing minimal loss in photocatalytic activity (**Figure 5.6c**). After 5 cycles of oxidative amidation of 4-nitrobenzylalcohol, no significant change in the UV-visible-DRS spectrum of PC-1 was observed (**Figure 5.6d**).

5.11. Conclusion

In summary, we successfully employed lead-free halide perovskites Cs_2CuBr_4 (PC-1 and PC-2), featuring distinct electronic properties and particle sizes, for the photocatalytic amidation

of alcohols. Structural variations between the two photocatalysts resulted in different band structures, with PC-1 exhibiting a more negative CBM and a more positive VBM compared to PC-2. These favorable band alignments in PC-1 facilitated photocatalytic O_2 reduction to form superoxide radicals, which help in the C–N coupling reaction.

Table 5.5. ^{1}H NMR and ^{13}C NMR spectra of the products.[5,6,7]

5a. phenyl(pyrrolidin-1-yl)methanone 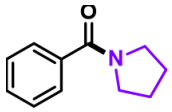	^{1}H NMR (500 MHz, $CDCl_3$) δ: 7.37 (dd, *J* = 69.7, 6.3 Hz, 5H), 3.56 (d, 2H), 3.33 (d, 2H), 1.83 (dt, 4H). ^{13}C NMR (126 MHz, $CDCl_3$) δ: 169.82, 137.12, 129.82, 128.25, 127.07, 49.64, 46.21, 26.37, 24.45. **Yield: 88% (77 mg and 0.44 mmol)**
5b. pyrrolidin-1-yl(p-tolyl)methanone 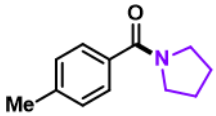	^{1}H NMR (500 MHz, $CDCl_3$) δ: 7.43 (d, *J* = 8.1 Hz, 2H), 7.20 (d, *J* = 7.9 Hz, 2H), 3.64 (d, 2H), 3.44 (d, 2H), 2.38 (s, 3H), 1.91 (dt, 4H). ^{13}C NMR (126 MHz, $CDCl_3$) δ: 169.92, 139.96, 134.19, 128.83, 127.22, 49.71, 46.25, 26.41, 24.46, 21.40. **Yield: 84% (80 mg and 0.42 mmol)**
5c. (4-methoxyphenyl)(pyrrolidin-1-yl)methanone 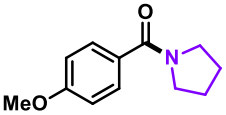	^{1}H NMR (500 MHz, $CDCl_3$) δ: 7.49 (d, *J* = 7.2 Hz, 2H), 6.87 (d, *J* = 7.2 Hz, 2H), 3.80 (s, 3H), 3.60 (dd, 2H), 3.45 (dd, 2H), 1.88 (dt, 4H). ^{13}C NMR (126 MHz, $CDCl_3$) δ: 169.45, 160.78, 129.41, 129.23, 113.35, 55.23, 49.79, 46.33, 26.47, 24.42. **Yield: 83% (80 mg and 0.41 mmol)**
5d. pyrrolidin-1-yl(3,4,5-trimethoxyphenyl)methanone 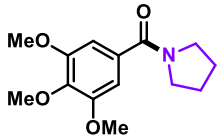	^{1}H NMR (500 MHz, $CDCl_3$) δ: 7.34 (d, *J* = 51.5 Hz, 2H), 3.95 (s, 9H), 3.89 (dd, 2H), 3.88 (dd, 2H) 1.52 (dt, 4H). ^{13}C NMR (126 MHz, $CDCl_3$) δ: 170.63, 152.97, 142.82, 124.32, 107.38, 61.04, 56.17, 29.71, 22.70. **Yield: 80% (106 mg and 0.40 mmol)**
5e. (4-nitrophenyl)(pyrrolidin-1-yl)methanone 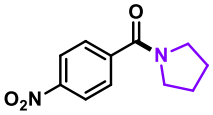	^{1}H NMR (500 MHz, $CDCl_3$) δ: 8.24 (d, *J* = 8.8 Hz, 2H), 7.66 (d, *J* = 8.8 Hz, 2H), 3.64 (t, 2H), 3.36 (t, 2H), 1.93 (dt, 4H). ^{13}C NMR (126 MHz, $CDCl_3$) δ: 167.52, 148.47, 143.11, 128.18, 123.80, 49.54, 46.48, 26.43, 24.42. **Yield: 97% (107 mg and 0.48 mmol)**
5f. (2-nitrophenyl)(pyrrolidin-1-yl)methanone 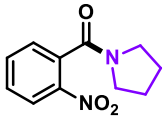	^{1}H NMR (500 MHz, $CDCl_3$) δ: 8.17 (d, *J* = 9.2 Hz, 1H), 7.71 (t, *J* = 8.1 Hz, 1H), 7.58 – 7.53 (m, 1H), 7.44 (d, *J* = 6.3 Hz, 1H), 3.70 (t, 2H), 3.15 (t, 2H), 1.95 (dt, 4H). ^{13}C NMR (126 MHz, $CDCl_3$) δ: 171.16, 166.18, 144.94, 134.02, 129.76, 128.18, 124.70, 48.22, 45.82, 25.81, 24.50. **Yield: 91% (101 mg and 0.46 mmol)**

5g. (4-chlorophenyl)(pyrrolidin-1-yl)methanone 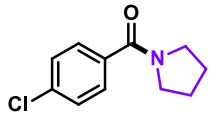	^{1}H NMR (500 MHz, $CDCl_3$) δ: 7.47 (d, *J* = 8.3 Hz, 2H), 7.38 (d, *J* = 8.4 Hz, 2H), 3.63 (d, 2H), 3.41 (d, 2H), 1.93 (dd, 4H). ^{13}C NMR (126 MHz, $CDCl_3$) δ: 168.68, 135.89, 135.39, 128.67, 128.53, 49.67, 46.36, 26.41, 24.41. **Yield: 95% (99 mg and 0.47 mmol)**
5h. pyrrolidin-1-yl(4-(trifluoromethyl)phenyl)methanone 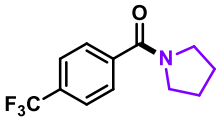	^{1}H NMR (500 MHz, $CDCl_3$) δ: 7.57 (d, *J* = 8.2 Hz, 4H), 3.57 (t, 2H), 3.30 (t, 2H), 1.84 (dt, 4H). ^{13}C NMR (126 MHz, $CDCl_3$) δ 168.11, 140.67, 131.57 (q, J_{C-F} = 32.4 Hz), 127.39 (q, J_{C-F} = 4.5 Hz), 125.02 (q, J_{C-F} = 240.00 Hz), 122.64, 49.36, 46.15, 26.22, 24.25. **Yield: 98% (120 mg and 0.49 mmol)**
5i. pyrrolidin-1-yl(2-(trifluoromethyl)phenyl)methanone 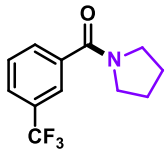	^{1}H NMR (500 MHz, $CDCl_3$) δ: 7.82 (s, 1H), 7.74 (d, *J* = 7.7 Hz, 1H), 7.69 (d, *J* = 7.9 Hz, 1H), 7.58 – 7.55 (m, 1H), 3.70 (t, 2H), 3.44 (t, 2H), 1.96 (dt, 4H). ^{13}C NMR (126 MHz, $CDCl_3$) δ: 168.80, 153.34, 151.99 (q, J_{C-F} = 34.33 Hz), 126.50 (d, J_{C-F} = 1.2 Hz), 121.04 (q, J_{C-F} = 3.2 Hz), 116.66 (q, J_{C-F} = 3.4 Hz), 113.97 (q, J_{C-F} = 269.9 Hz), 111.75, 47.83, 25.18. **Yield: 83% (100 mg and 0.41 mmol)**
5j. pyrrolidin-1-yl(thiophen-2-yl)methanone 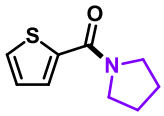	^{1}H NMR (500 MHz, $CDCl_3$) δ: 7.54 (d, *J* = 3.7 Hz, 1H), 7.49 (d, *J* = 5.0 Hz, 1H), 7.09 (t, 1H), 3.73 (dt, 4H), 1.99 (dd, 4H). ^{13}C NMR (126 MHz, $CDCl_3$) δ: 161.90, 139.45, 129.63, 127.13, 48.98, 47.39, 26.74, 24.10. **Yield: 82% (74 mg and 0.41 mmol)**
5k. pyridin-2-yl(pyrrolidin-1-yl)methanone 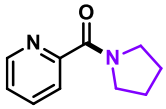	^{1}H NMR (500 MHz, $CDCl_3$) δ: 8.51 (s, 1H), 7.73 (d, *J* = 6.7 Hz, 2H), 7.28 (s, 1H), 3.63 (dd, 4H), 1.85 (dd, 4H). ^{13}C NMR (126 MHz, $CDCl_3$) δ: 166.52, 154.39, 147.97, 136.83, 124.68, 123.67, 49.05, 46.78, 26.51, 23.98. **Yield: 84% (74 mg and 0.42 mmol)**
5l. 3-(4-nitrobenzoyl)oxazolidin-2-one 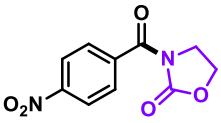	^{1}H NMR (500 MHz, DMSO) δ: 8.33 (d, *J* = 8.9 Hz, 1H), 8.18 (d, *J* = 9.0 Hz, 1H), 3.36 (s, 2H). ^{13}C NMR (126 MHz, DMSO) δ: 172.67, 157.68, 147.83, 140.52, 128.97, 124.40, 64.76, 41.84. **Yield: 78% (92 mg and 0.39 mmol)**
5m. (4-nitrophenyl)(piperidin-1-yl)methanone 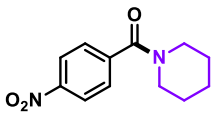	^{1}H NMR (500 MHz, $CDCl_3$) δ: 8.28 (d, *J* = 8.8 Hz, 2H), 7.57 (d, *J* = 8.8 Hz, 2H), 3.51 (d, 4H), 1.62 (d, 6H). ^{13}C NMR (126 MHz, $CDCl_3$) δ: 167.95, 148.18, 142.66, 127.79, 123.90, 48.67, 43.23, 26.51, 25.50, 24.39. **Yield: 88% (111 mg and 0.47 mmol)**
5n. morpholino(4-nitrophenyl)methanone 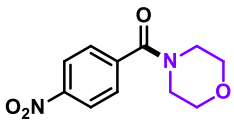	^{1}H NMR (500 MHz, $CDCl_3$) δ: 8.30 (d, *J* = 8.8 Hz, 2H), 7.60 (d, *J* = 8.8 Hz 2H), 3.75 (dd, 4H). ^{13}C NMR (126 MHz, $CDCl_3$) δ: 168.13, 148.50, 141.38, 128.14, 123.96, 66.73, 48.06. **Yield: 79% (93 mg and 0.39 mmol)**

5o. 4-nitro-N-(pyridin-2-yl)benzamide 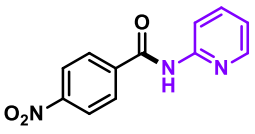	^{1}H NMR (500 MHz, DMSO) δ: 11.19 (s, 1H), 8.41 (s, 1H), 8.34 (d, *J* = 8.9 Hz, 2H), 8.23 (d, *J* = 8.9 Hz, 3H), 7.88 (s, 1H), 7.21 (s, 1H). ^{13}C NMR (126 MHz, DMSO) δ: 165.07, 152.30, 149.77, 148.48, 140.35, 138.68, 130.12, 123.81, 120.73, 115.37. **Yield: 76% (92 mg and 0.38 mmol)**
5p. 4-nitro-N-phenylbenzamide 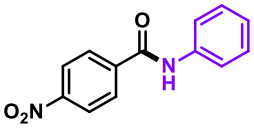	^{1}H NMR (500 MHz, $CDCl_3$) δ: 8.58 (s, 1H), 8.37 (dd, *J* = 12.2, 8.7 Hz, 2H), 8.09 (dd, *J* = 8.8, 3.5 Hz, 2H), 7.44 (d, *J* = 7.5 Hz, 2H), 7.29 (dd, *J* = 11.1, 9.9 Hz, 3H). ^{13}C NMR (126 MHz, $CDCl_3$) δ: 169.42, 150.93, 141.59, 140.06, 130.46, 129.36, 127.10, 124.00, 120.99. **Yield: 74% (90 mg and 0.37 mmol)**
5q. N-benzylbenzamide 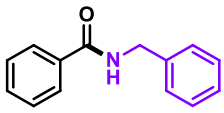	^{1}H NMR (500 MHz, $CDCl_3$) δ 7.82 (d, *J* = 7.1 Hz, 2H), 7.52 (t, *J* = 7.4 Hz, 1H), 7.45 (t, *J* = 7.5 Hz, 2H), 7.38 (d, *J* = 4.4 Hz, 4H), 7.33 (d, *J* = 4.4 Hz, 1H), 6.53 (s, 1H), 4.67 (d, *J* = 5.7 Hz, 2H). ^{13}C NMR (126 MHz, $CDCl_3$) δ 167.41, 138.20, 134.40, 131.59, 128.81, 128.62, 127.94, 127.65, 127.03 126.99 44.16. **Yield: 71% (62 mg and 0.35 mmol)**
5r. N,N-diethyl-4-nitrobenzamide 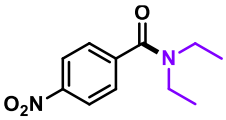	^{1}H NMR (500 MHz, $CDCl_3$) δ 8.36 (d, *J* = 8.92 Hz, 2H), 8.13 (d, *J* = 8.7 Hz, 2H), 3.45 (q, 2H), 3.27 (q, 2H), 1.27 (t, 6H). ^{13}C NMR (126 MHz, $CDCl_3$) δ 171.31, 140.02, 137.32, 129.07, 128.38, 126.28, 43.29, 39.34, 14.15, 13.00. **Yield: 66% (73 mg and 0.32 mmol)**

5.12. ^{1}H NMR and ^{13}C NMR spectra of the product

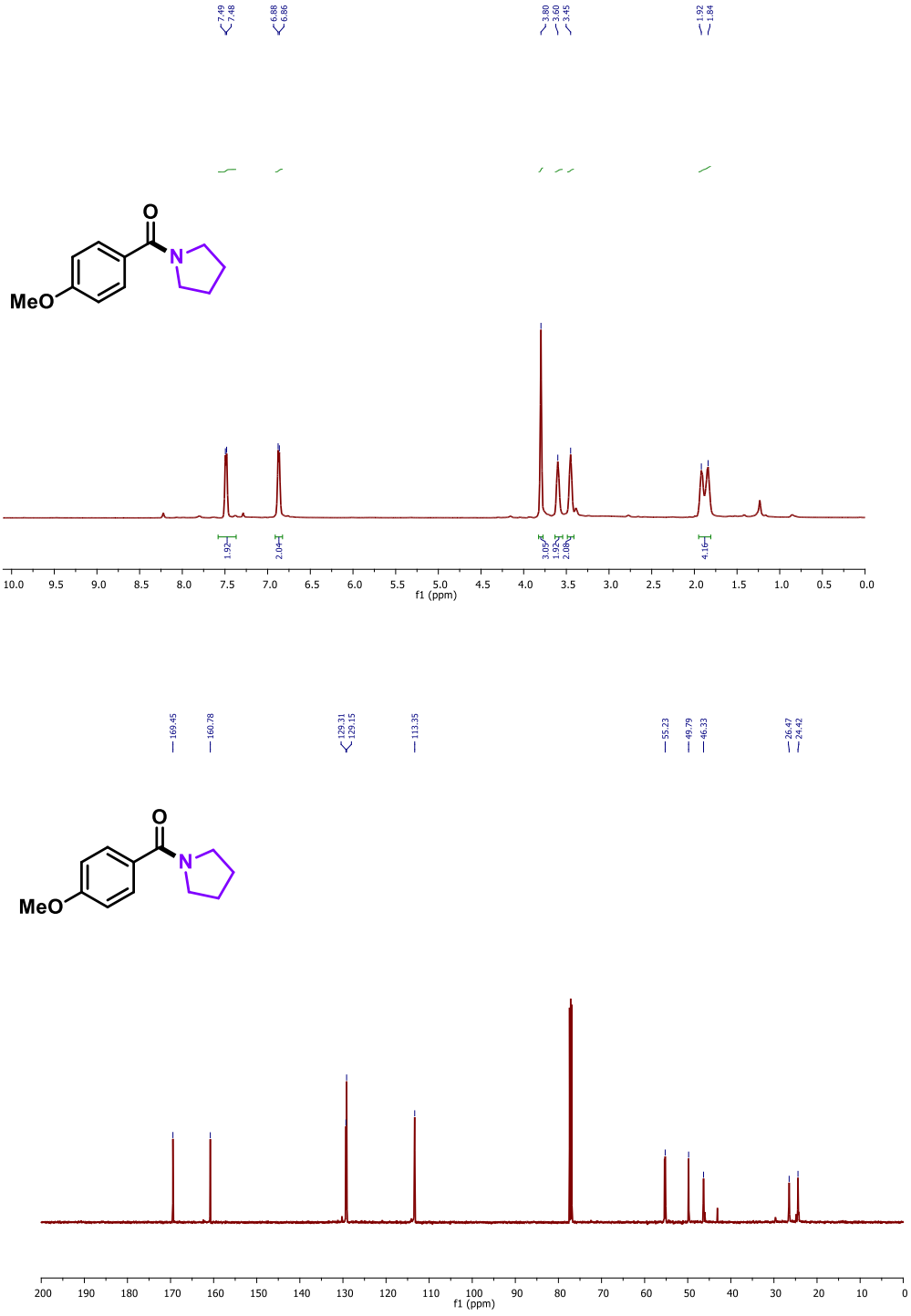

Figure 5.7: ^{1}H NMR and ^{13}C NMR spectra of the compound 5c.

5.13. References

1 S. Das, S. Mondal, S. P. Midya, S. Mondal, E. Ghosh and P. Ghosh, *J. Org. Chem.*, 2023, **88**, 14847–14859.

2 S. Gaspa, A. Farina, M. Tilocca, A. Porcheddu, L. Pisano, M. Carraro, U. Azzena and L. De Luca, *J. Org. Chem.*, 2020, **85**, 11679–11687.

3 V. Vyas, V. Kumar and A. Indra, *Chem. Commun.*, 2024, **60**, 2544–2547.

4 B. Goel, V. Vyas, N. Tripathi, A. Kumar Singh, P.W. Menezes, A. Indra, and S.K. Jain, *ChemCatChem*, 2024, **12**, 5743-5749.

5 J. Kweon, B. Park, D. Kim and S. Chang, *Nat. Commun.*, 2024, **15**, 3788.

6 X. Chen, Z. Lian and S. Kramer, , *Angew. Chem. Int. Ed*, 2023, **135**, e202217638.

7 H. Ghafuri, M. G. Gorab and H. Dogari, *Sci. Rep.*, 2022, **12**, 2331.

8 B. Lu, W.L. Xiao, and J.R. Chen, *Molecules*, 2022, **27**, 517.

9 J. Liu, C. Zhang, Z. Zhang, X. Wen, X. Dou, J. Wei, X. Qiu, S. Song and N. Jiao, *Science,* 2020, **367**, 281–285.

10 A. Hassan Tolba, M. Krupička, J. Chudoba and R. Cibulka, *Org. Lett.*, 2021, **23**, 6825–6830.

11 X. Zhu, Y. Lin, J. San Martin, Y. Sun, D. Zhu and Y. Yan, *Nat. Commun.*, 2019, **10**, 4279.

12 N. J. Oldenhuis, V. M. Dong and Z. Guan, *Tetrahedron*, 2014, **70**, 4213–4218.

13 L. Deng, L. Chen, L. Zhu, Y. Li, J. Ou-Yang, S. Wu, P. Chen, S. Shen, J. Guo, Y. Zhou, C. T. Au and S. F. Yin, *Chem. Eng. Sci.*, 2022, **261**, 117960.

14 A. Rashidizadeh, H. Ghafuri, N. Goodarzi and N. Azizi, *Solid State Sci.*, 2020, **109**, 106427.

15 D. Leow, *Org. Lett.*, 2014, **16**, 5812–5815.

16 Z. Akrami, and M. Hosseini-Sarvari, *Europ. J. Org. Chem.*, 2022, e202200429.

17 F. K. C. Leung, J. F. Cui, T. W. Hui, K. K. Y. Kung and M. K. Wong, *Asian J. Org. Chem.*, 2015, **4**, 533–536.

18 Y. Long, J. Wen, L. Zhu, L. Zeng, M. Lu, and L. Deng., *J. Photochem. Photobio. A: Chem.*, 2024. **453**, 115612.

19 A. Dey, S. Chakraborty, A. Singh, F. A. Rahimi, S. Biswas, T. Mandal, and T.K. Maji, *Angew. Chem. Int. Ed.*, 2024, e202403093.

20 V. Kumar, S. K. Patel, V Vyas, D. Kumar, E. S. S. Iyer, and A. Indra, *Chem. Sci.*, 2024, **15**, 13218-13226

21 J. P. Stephenson, J. E. Patterson, W. Huang, D. D. Dlott, J. G. Fujimoto, E. P. Ippen, P. B. Davies, T. H. Ong, R. N. Ward, M. Hara, H. Sasabe, K. Wolfgang, C. Kodama, H. Sumida, H. Nozoye, S. Lagutchev, D. G. Cahill, P. V. Braun, R. Segalman, A. Majumdar, M. T. Seidel, H. Zewail, and F. Seitz, *Science*, 2007, **317**, 790–792.

22 A. Kumar, N. A. Espinosa-Jalapa, G. Leitus, Y. Diskin-Posner, L. Avram and D. Milstein, *Angew. Chemie - Int. Ed.*, 2017, **56**, 14992–14996.

23 V. Vyas, P. Maurya and A. Indra, *Chem. Sci.*, 2023, **14**, 12339–12344.

24 H. Huang, B. Pradhan, J. Hofkens, M. B. J. Roeffaers and J. A. Steele, *ACS Energy Lett.*, 2020, **5**, 1107–1123.

25 P. Zhang, Y. Tong, Y. Liu, J. J. M. Vequizo, H. Sun, C. Yang, A. Yamakata, F. Fan, W. Lin, X. Wang and W. Choi, *Angew. Chem. Int. Ed.*, 2020, **59**, 16209–16217.

26 Y. Dai, C. Poidevin, C. Ochoa-Hernández, A. A. Auer and H. Tüysüz, *Angew. Chem. Int. Ed.*, 2020, **132**, 5837–5845.

27 Y. Li, Y. Gao, Z. Deng, Y. Cao, T. Wang, Y. Wang, C. Zhang, M. Yuan and W. Xie, *Nat. Commun.,* 2023*,* **14***,* 4673.

28 K. Mishra, D. Guyon, J. San Martin and Y. Yan, *J. Am. Chem. Soc.*, 2023, **145**, 17242–17252.

29 Y. Li, T. Wang, Y. Wang, Z. Deng, L. Zhang, A. Zhu, Y. Huang, C. Zhang, M. Yuan and W. Xie, *ACS Catal.* , 2022, **12**, 5903–5910.

30 I. Rosa-Pardo, D. Zhu, A. Cortés-Villena, M. Prato, L. De Trizio, L. Manna, R. E. Galian and J. Pérez-Prieto, *ACS Energy Lett.*, 2023, **8**, 2789–2798.

31 H. Jiang, M. Liu, X. Lian, M. Zhu and F. Zhang, *Angew. Chem. Int. Ed.,* 2024, **136,** 202318850.

32 J. Sheng, Y. He, M. Huang, C. Yuan, S. Wang and F. Dong, *ACS Catal.*, 2022, **12**, 2915–2926.

33 T. Yan, N. Li, L. Wang, W. Ran, P. N. Duchesne, L. Wan, N. T. Nguyen, L. Wang, M. Xia, and G. A. Ozin, *Nat. Commun.*, 2020, **11**, 6095.

34 S. Zhang, Z. Q. Huang, Y. Ma, W. Gao, J. Li, F. Cao, L. Li, C. R. Chang and Y. Qu, *Nat. Commun.*, 2017, **8**, 15266.

35 T. Cai, W. Shi, S. Hwang, K. Kobbekaduwa, Y. Nagaoka, H. Yang, K. Hills-Kimball, H. Zhu, J. Wang, Z. Wang, Y. Liu, D. Su, J. Gao and O. Chen, *J. Am. Chem. Soc.*, 2020, **142**, 11927–11936.

36 P. Cheng, L. Sun, L. Feng, S. Yang, Y. Yang, D. Zheng, Y. Zhao, Y. Sang, R. Zhang, D. Wei, W. Deng and K. Han, *Angew. Chem. Int. Ed.*, 2019, **58**, 16087–16091.

37 J. He, W. H. Fang, R. Long and O. V. Prezhdo, *J. Am. Chem. Soc.*, 2020, **142**, 14664–14673.

38 L. Qiao, W. H. Fang, O. V. Prezhdo and R. Long, *J. Am. Chem. Soc.*, 2022, **144**, 5543–5551.

39 T. Wang, Y. Li, X. Yang, Y Hu, X. Du, M. Zhang, Z. Huang, S. Liu, Y. Wang, and W. Xie, *Angew. Chem. Int. Ed.* 2024, e202409656.

40 Z. Zhang, D. Li, H. Hu, Y. Chu and J. Xu, *Inorg. Chem.*, 2023, **62**, 9240–9248.

41 Z. Zhang, D. Li, Y. Chu, L. Chang, and J. Xu, *J. Phys. Chem. Lett.*, 2023, **14**, 5249–5259.

42 R. Grisorio, F. Fasulo, A. B. Muñoz-García, M. Pavone, D. Conelli, E. Fanizza, M. Striccoli, I. Allegretta, N. Margiotta, P. Vivo and G. P. Suranna, *Nano Lett.*, 2022, **22**, 4437–4444.

43 J. Qian, H. Hu, Y. Liang and Z. Zhang, *Appl. Surf. Sci.*, 2024, **648**, 159084.

44 Z. Zhang, X. Wang, J. Qian and J. Xu, *J. Energy Chem.*, 2024, **92**, 521–533.

45 H. Tang, X. Wang, C. Yao and Z. Zhang, *Sep. Purif. Technol.*, 2024, **338**, 126544.

46 A. Hankin, F. E. Bedoya-Lora, J. C. Alexander, A. Regoutz and G. H. Kelsall, *J. Mater. Chem. A*, 2019, **7**, 26162–26176.

47 Y. Wang, A. Vogel, M. Sachs, R. S. Sprick, L. Wilbraham, S. Moniz, R. Godin, M. A. Zwijnenburg, J. R. Durrant, A. I. Cooper and J. Tang, *Nat. Energy*, 2019, **4**, 746–760.

48 Y. T. Xiong, W. X. Liu, L. Tian, P. L. Qin, X. B. Chen, L. Ma, Q. B. Liu, S. J. Ding and Q. Q. Wang, *Adv. Funct. Mater.*, 2024, **2407819**, 2407819.

49 Y. Wang, R. Godin, J.R. Durrant, and J. Tang. *Angew. Chem. Int. Ed.*, 2021, **60**. 20811-20816.

50 A. Indra, R. Beltrán-Suito, M. Müller, R. P. Sivasankaran, M. Schwarze, A. Acharjya, B. Pradhan, J. Hofkens, A. Brückner, A. Thomas, P. W. Menezes and M. Driess, *ChemSusChem*, 2021, **14**, 306–312.

51 J. Yang, A. Acharjya, M. Ye, J. Rabeah, Z. Kochovski, S. Youk, J. Roeser, J. Grüneberg, C. Penschke, and M. Schwarze, *Angew. Chem. Int. Ed.*, 2021, **60**, 19797-19803.

52 A. Indra, A. Acharjya, P.W. Menezes, D. Hollmann, M. Schwarze, M. Aktas, A. Friedrich, S. Lochbrunner, A. Thomas, and M. Driess, *Angew. Chem. Int. Ed.* 2017*,* **56,** 1653-1657.

53 J. Zhang, W. Ling, A. Li, J. Ma, M. Hong and R. Sun, *Adv. Funct. Mater.*, 2024, **e**2405420.

54 X. Wang, B. Liu, S. Ma, Y. Zhang, L. Wang, G. Zhu, W. Huang and S. Wang, *Nat. Commun.*, 2024, **15**, 2600.

55 M. Roy, B. Mishra, S. Maji, A. Sinha, S. Dutta, S. Mondal, A. Banerjee, P. Pachfule, and D. Adhikari, *Angew. Chem. Int. Ed.*, 2024, e202410300.

56 M. Y. Qi, Y. H. Li, M. Anpo, Z. R. Tang and Y. J. Xu, *ACS Catal.*, 2020, **10**, 14327–14335.

57 H. Wang, W. Lu, P. Xu, J. Luo, K. Yao, J. Zhang, X. Wei, S. Peng, H. Cheng, H. Hu and K. Sun, *ACS Sustain. Chem. Eng.*, 2023, **11**, 5963–5972.

58 Q. Fan, D. Liu, Z. Xie, Z. Le, H. Zhu and X. Song, *J. Org. Chem.*, 2023, **88**, 14559–14570.

59 M. Xiao, M. Hao, M. Lyu, E. G. Moore, C. Zhang, B. Luo, J. Hou, J. Lipton-Duffin and L. Wang, *Adv. Funct. Mater.*, 2019, **29**, 1905683.

60 K. Michalec, B. Mozgawa, A. Kusior, P. Pietrzyk, Z. Sojka and M. Radecka, *J. Phys. Chem. C*, 2024, **128**, 5011–5029.

61 Q. Fan, H. Zhang, D. Liu, H. Zhu, Z. Xie and Z. Le, *J. Org. Chem.*, 2023, **88**, 7391–7400.

62 I. Rosa-Pardo, C. Casadevall, L. Schmidt, M. Claros, R. E. Galian, J. Lloret-Fillol and J. Pérez-Prieto, *Chem. Commun.*, 2020, **56**, 5026–5029.

63 Y. Deng, W. Liu, R. Xu, R. Gao, N. Huang, Y. Zheng, Y. Huang, H. Li, X. Y. Kong and L. Ye, *Angew. Chem. Int. Ed.*, 2024, e202319216.

64 J. Luo, X. Wei, Y. Qiao, C. Wu, L. Li, L. Chen, and J. Shi, *Adv. Mater.*, 2023, **35**, 2210110.

65 A. K. Singh, K. Bijalwan, N. Kaushal, A. Kumari, A. Saha and A. Indra, *ACS Appl. Nano Mater.*, 2023, **6**, 8036–8045.

66 A. K. Singh, D. Hollmann, M. Schwarze, C. Panda, B. Singh, P. W. Menezes and A. Indra, *Adv. Sustain. Syst.*, 2021, **5**, 2000288.

67 O. C. Compton and F. E. Osterloh, *J. Phys. Chem. C*, 2009, **113**, 479–485.

68 E. S. Jang, C. L. Mcmullin, M. Käß, K. Meyer, T. R. Cundari and T. H. Warren, *J. Am. Chem. Soc.* 2014, **136**, 10930−10940.

69 W. P. Carson, A. V. Tsymbal, R. W. Pipal, G. A. Edwards, J. R. Martinelli, A. Cabré and D. W. C. MacMillan, *J. Am. Chem. Soc.*, 2024, **146**, 15681–15687.

70 E. Boess, C. Schmitz and M. Klussmann, *J. Am. Chem. Soc.*, 2012, **134**, 5317–5325.